Filtering Antenna Array Based on Corrugated Vivaldi Elements

Matti Kuosmanen, Jari Holopainen, Juha Ala-Laurinaho, Tero Kiuru, and Ville Viikari, *Senior Member, IEEE*

***Abstract*— This article presents a bandpass filtering antenna array based on corrugated Vivaldi antenna elements and finline waveguides. The low-pass section of the filtering antenna element is realized by periodically corrugating the inner edges of the Vivaldi elements. The structure can be considered as a periodic transmission line that inherently acts as a low-pass filter. The high-pass section of the filtering element is realized by surrounding the corrugated slotline with a waveguide. The resulting antenna structure, a finline-fed Vivaldi element, exhibits a wide 1.2–3.1-GHz bandpass response with the upper band-stop rejection exceeding 20 dB up to 6 GHz. The filtering properties are almost independent of the scan angle. The active reflection coefficient is <−10 dB with beam-steering angles within $\theta = \pm 60°$ in the E- and D-planes and <−6 dB in the H-plane. The operation of the filtering antenna element is confirmed by periodic unit-cell simulations and measuring a manufactured 6 × 6 array prototype.**

***Index Terms*— Antenna array, bandpass filter, corrugation, filtering antenna, finline, periodic transmission line (TL), Vivaldi, wideband.**

I. Introduction

RADIO systems, such as radars, electronic warfare equipment, and mobile communication devices, need filters to meet the strict requirements for their out-of-band emissions. Filters are also needed in reception to protect the receiver from saturating out-of-band signals. These signals may be a problem, for example, with high-sensitivity devices such as signal intelligence receivers.

Conventionally, the out-of-band emissions are filtered out using external filters in different positions in the signal chain, and they may be large and expensive. Furthermore, in the case of active antenna arrays, one filter stage is needed between each antenna element and transmitter/receiver (T/R) module in order to filter out unwanted spectral components. If the antenna elements are densely spaced in a conventional half-wavelength lattice, the space for a high-performance filter and other transceiver components is very limited.

To improve the integration level and compactness of radio systems, many studies have proposed antenna-integrated filters or filtering antennas. There are multiple ways to implement the functionality of the filtering antenna, and they have been recently reviewed in [1]. Most research has concentrated on single filtering antennas, whereas the filtering antenna arrays have gained less attention. However, a few good examples of filtering microstrip antenna arrays [2], [3], [4], [5], [6], [7], [8], [9], cavity-resonator-based filtering arrays [10], [11], [12], and slot/waveguide aperture antenna arrays with waveguide filters [13], [14], [15] have been reported. Many of these filtering arrays, however, have only a few elements and the scalability of some arrays is uncertain. The integrated filter has to fit into the lattice of the antenna array in order to guarantee its scalability. Furthermore, in some filtering arrays, e.g., in [15], the filter is an integral part of the feeding network of multiple elements, and the applicability of the technique is not known in the beam-steering scenario.

In this article, we investigate a new type of filtering antenna array, in which bandpass filters are integrated into wideband Vivaldi elements. The filtering antenna element employs a periodically loaded slotline to realize the low-pass filter (LPF) and a waveguide to realize the high-pass filter (HPF). As a result, the structure can be treated as a periodically loaded finline. The steep low-pass response of the periodic slotline in combination with a natural high-pass response of the waveguide provides exceptional bandpass performance for the filtering antenna, which is almost independent of the scan angle. Furthermore, the scalability of the antenna array is guaranteed since the filtering antenna element can fit into a regular half-wavelength array lattice. This kind of filtering array can be used, for example, in wideband signal intelligence systems in electronic warfare.

The low-pass section of the proposed filtering antenna is based on the corrugated slotline. The spectral properties of these kinds of periodic structures have been extensively studied during past decades. Depending on the publication and application, they have been called by different names. In [16], [17], and [18], these are called periodic transmission lines (TLs) due to their periodic nature. In these classical works, the TL characteristics, such as impedance, dispersion, and propagation coefficient, have been studied for different TLs from the circuit and TL theory point of view.

Manuscript received 27 January 2023; revised 11 April 2023; accepted 6 May 2023. Date of publication 26 May 2023; date of current version 4 August 2023. This work was supported by Saab AB. The work of Matti Kuosmanen was supported by the Finnish Foundation for Technology Promotion. *(Corresponding author: Matti Kuosmanen.)*

Matti Kuosmanen is with the Department of Electronics and Nanoengineering, Aalto University, 02150 Espoo, Finland, and also with Saab Finland Oy, 00100 Helsinki, Finland (e-mail: matti.s.kuosmanen@aalto.fi).

Jari Holopainen, Juha Ala-Laurinaho, and Ville Viikari are with the Department of Electronics and Nanoengineering, Aalto University, 02150 Espoo, Finland.

Tero Kiuru is with Saab Finland Oy, 00100 Helsinki, Finland.

Color versions of one or more figures in this article are available at https://doi.org/10.1109/TAP.2023.3278879.

Digital Object Identifier 10.1109/TAP.2023.3278879

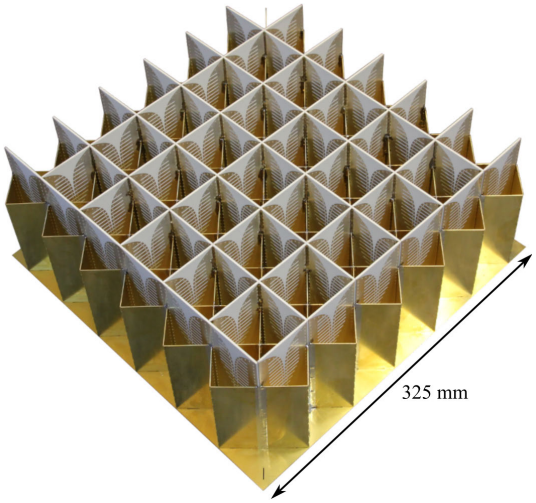

Fig. 1. Manufactured 6 × 6 dual-polarized antenna array.

In recent years, following the success of the research of one-wire spoof surface plasmon polariton (SSPP) TLs [19], also multiwire TLs and periodic waveguides are published under the SSPP terminology. For example, in [20], the corrugated slotline was used in a differential bandpass filter and called an odd-mode SSPP TL. In [21], a substrate-integrated waveguide (SIW) with via-based diaphragms was proposed as a bandpass filter. The similarity of the SSPP TLs and classical periodic TLs was recognized in [22], where a conventional periodically loaded stripline filter was investigated and compared to SSPP TLs.

The periodic TLs, more precisely corrugated slotlines or differential parallel-plate lines, have been used to feed a Vivaldi element in several studies, such as in [23], [24], [25], and [26]. In some of these works, the objective was to demonstrate the usability of periodic TLs to feed the antenna, and some works also recognize and exploit their filtering effect. However, these are only single antenna elements. In [27], the periodic Vivaldi elements were used in an antenna array, but the intention was not to exploit their low-pass functionality but to improve the polarization performance of the array. To the authors' knowledge, corrugated Vivaldi elements with waveguides have not been previously used in antenna arrays for bandpass filtering purposes. Corrugated slotlines have only been used in planar filters, and this work introduces a new method to integrate the filter into an antenna array and to prevent detrimental radiation of the filter structure.

The rest of this article is constructed as follows. First, the operating principle and structure of the filtering antenna element are investigated in detail. After that, the performance of the antenna array is comprehensively analyzed based on the unit-cell simulations (infinite array approximation). Third, the obtained simulation results are verified by measuring a manufactured prototype, as shown in Fig. 1. Finally, this article concludes by summarizing the main results and proposing further research.

II. Antenna Structure and Operating Principle

The antenna array is based on traditional Vivaldi elements [28], which have been used in antenna arrays already for decades. The structure of one antenna element is presented in Fig. 2 with the corresponding dimensions in Table I. Here, one can distinguish three functional parts that construct the filtering radiator:

1) Vivaldi antenna element;
2) corrugation in the slotline;
3) waveguide around the slotline, which together form a finline.

The Vivaldi element, i.e., exponentially tapered slotline, acts as a wideband electromagnetic radiator. The corrugation in the slotline makes it an LPF. The square waveguide is placed around the antenna element in order to realize an HPF. Together with the slotline, the waveguide constructs a finline structure [29], whose cutoff frequency defines the high-pass frequency.

In the following, the structure and operational principle of these parts, and their combination, are discussed in detail.

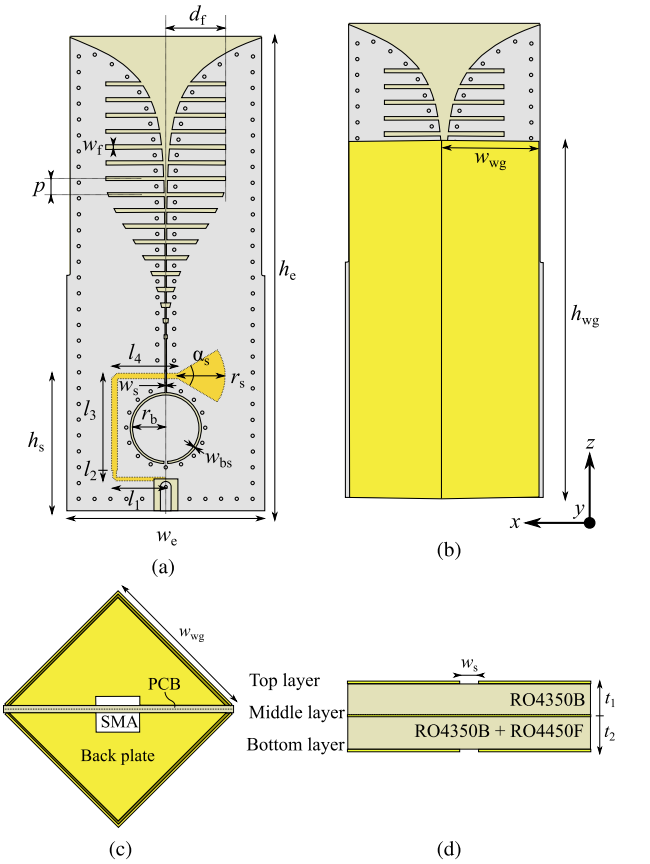

Fig. 2. Structure of one antenna element. (a) Side view without a waveguide. (b) Side view with the waveguide. (c) Top view. (d) Cross section of the PCB.

A. Vivaldi Element

The antenna element is based on a conventional PCB-based Vivaldi antenna. The Vivaldi element is manufactured on a three-layer PCB, which contains the Vivaldi pattern on the top and bottom sides of the PCB [Fig. 2(a)].

The feeding structure, comprised of a stripline and radial stub, is placed on the middle layer, as shown in Figs. 2(a) and 2(d). The unbalanced feedline is transformed into balanced slotline using circular balun. However, in contrast to typical designs, the balun hole is mostly filled with

TABLE I
DIMENSIONS OF THE PROPOSED ANTENNA

Parameter	Description	Value
α_s	Angle of the radial stub	66°
d_f	Depth of the filter slot	15.1 mm
h_e	Height of the element	120 mm
h_s	Height position of the stripline	34 mm
l_1	1st length of the stripline	13 mm
l_2	2nd length of the stripline	2.0 mm
l_3	3rd length of the stripline	24 mm
l_4	4th length of the stripline	16 mm
p	Period of the corrugation	4 mm
R	Exponential curve parameter	0.12
r_b	Radius of the balun	17.5 mm
r_s	Radius of the radial stub	12 mm
t_1	Substrate layer 1 thickness	0.762 mm
t_2	Substrate layer 2 thickness	0.799 mm
$w_{1,sl}$	1st width of the stripline	1.3 mm
$w_{2,sl}$	2nd width of the stripline	0.8 mm
w_{bs}	Balun slot width	0.50 mm
w_e	Element spacing/width	50 mm
w_f	Width of the filter slot	1.0 mm
w_s	Slot width	0.25 mm
w_{wg}	Inner width of the waveguide	35 mm

copper to keep the copper cladding uniform. According to simulations, this does not affect the filter response. This kind of feeding structure is previously well described, e.g., in [30].

The whole PCB is manufactured of Rogers RO4350B laminate ($\epsilon_r = 3.66$ and $\tan\delta = 0.0037$ at 10 GHz), RO4450F prepreg ($\epsilon_r = 3.52$ and $\tan\delta = 0.004$ at 10 GHz), and standard 18-μm copper cladding. The top and bottom layers are finished with silver plating.

The height h_e of the Vivaldi element described in Fig. 2(a) is 120 mm ($1.2\lambda_{high}$, where λ_{high} is the wavelength at 3.0 GHz), including the height of the balun. The height of the bare Vivaldi element is 86 mm or $0.86\lambda_{high}$. According to [31], the Vivaldi element of this height should provide approximately a fractional bandwidth of 5:1. The width w_e of the elements is 50 mm, which corresponds to $\lambda_{high}/2$ spacing when the elements are placed next to each other.

The exponential opening of the flare is defined by the well-known formula [30]

$$y = c_1 e^{Rz} + c_2 \tag{1}$$

with

$$c_1 = \frac{y_2 - y_1}{e^{Rz_2} - e^{Rz_1}} \text{ and } c_2 = \frac{y_1 e^{Rz_2} - y_2 e^{Rz_1}}{e^{Rz_2} - e^{Rz_1}} \tag{2}$$

where (y_1, z_1) and (y_2, z_2) are the coordinates of the starting and end points of the exponential curve, respectively, and R is the curve parameter.

Both sides of the PCB are connected by vias in order to prevent internal resonances that cause impedance anomalies [32]. The antenna element is fed by a standard end-launch SMA connector (not shown in the figure).

B. Corrugation in the Slotline

The low-pass filtering of the proposed antenna element is based on a periodically loaded slotline. In general, the periodic TL can be modeled as a TL, which has periodically placed series impedance blocks (or shunt admittance blocks),

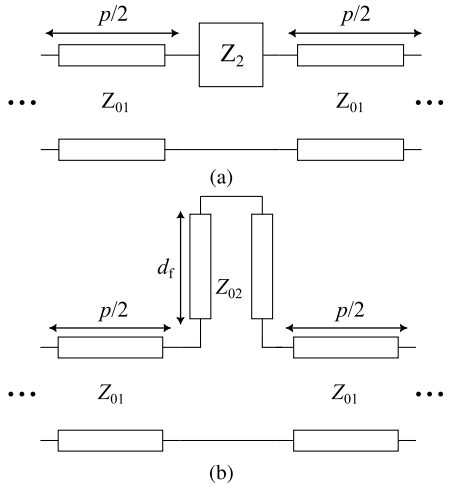

Fig. 3. (a) TL model of a general periodic TL loaded with lumped series impedance block. (b) TL model of asymmetric stub-loaded slotline. Both schematics illustrate one unit cell of the periodic structure.

as shown in Fig. 3(a) [16]. One unit cell of the lossless, periodic TL can be conveniently described by its ABCD parameters [17]

$$\begin{bmatrix} A & B \\ C & D \end{bmatrix} = \begin{bmatrix} \cos(\beta_1 p/2) & j\sin(\beta_1 p/2) \\ j\sin(\beta_1 p/2) & \cos(\beta_1 p/2) \end{bmatrix} \begin{bmatrix} 1 & \bar{Z}_2 \\ 0 & 1 \end{bmatrix} \times \begin{bmatrix} \cos(\beta_1 p/2) & j\sin(\beta_1 p/2) \\ j\sin(\beta_1 p/2) & \cos(\beta_1 p/2) \end{bmatrix}. \tag{3}$$

Here, TLs of length $p/2$ and lumped impedances $\bar{Z}_2$ are cascaded together such that $\bar{Z}_2$ is assumed to be in the middle of the TL. β_1 is the propagation constant in the unloaded TL. All impedances are normalized to the characteristic impedance of the unloaded TL (Z_{01}), and the normalization is denoted by a bar ($\bar{Z}$).

The dispersion characteristic of the periodic TL can be studied by formulating an eigenmode problem from the ABCD parameters [17]. It can be shown that the wavelength in the TL with series impedance blocks can be obtained from [16]:

$$\cos\frac{2\pi p}{\lambda_g} = \cos\frac{2\pi p}{\lambda_1} + j\frac{Z_2}{2Z_{01}}\sin\frac{2\pi p}{\lambda_1} \tag{4}$$

where λ_g is the guide wavelength in the loaded TL and λ_1 is the wavelength in the unloaded TL.

The impedance block of the periodic TL can be implemented by lumped or distributed elements. In the case of a corrugated slotline, the corrugations can be modeled as short-circuited serial stubs, as shown in Fig. 3(b). Note that the stubs are only on one side: Based on the image principle, the symmetrical two-sided periodic TL can be modeled by a one-sided equivalent circuit. The impedance of the stubs is [18]

$$Z_2 = jZ_{02}\tan\frac{2\pi d_f}{\lambda_2} \tag{5}$$

where Z_{02} is the characteristic impedance of the stub, λ_2 is the wavelength in the stub, and d_f is the length of the stub. By combining (4) and (5), we get the dispersion relation for

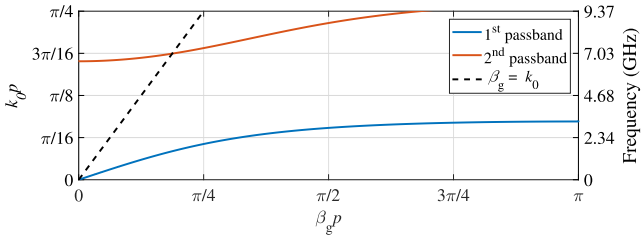

Fig. 4. Analytical $\beta_g p - k_0 p$ curve of the ideal corrugated slotline. The effective length of the stubs is ca. 20 mm, which corresponds to the effective length of the stub in the proposed antenna element. Dispersion curves of two first passbands are shown.

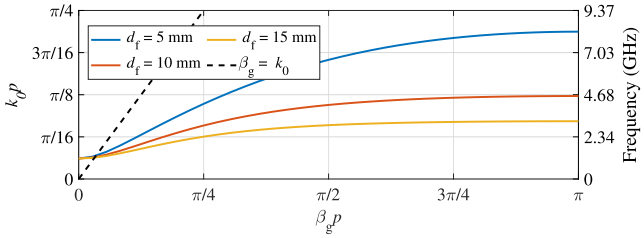

Fig. 5. $\beta_g p - k_0 p$ diagram of the proposed corrugated finline with different stub lengths d_f. The width of the slotline is 0.77 mm, corresponding to the dimensions of the corrugated Vivaldi element at the location of the deepest stub. Other dimensions are shown in Table I.

a one-sided corrugated slotline [16]

$$\cos\frac{2\pi p}{\lambda_g} = \cos\frac{2\pi p}{\lambda_1} - \frac{Z_{02}}{2Z_{01}}\tan\frac{2\pi d_f}{\lambda_2}\sin\frac{2\pi p}{\lambda_1}. \tag{6}$$

The dispersion characteristics of the corrugated slotline are shown in Fig. 4. The dispersion curve is based on the analytical formula (6), and it describes the relationship between the propagation constant β_g and the wavenumber of free space k_0. The lowest order propagating mode is described by the lowest part of the diagram. It can be seen that the corrugation shortens the wavelength of the propagating wave, and above the cutoff frequency, the wave propagation stops entirely. The first cutoff frequency of the periodic TL occurs when $\lambda_g = 2p$ [16]. This cutoff frequency is smaller than the first resonance frequency of the short-circuited stub (i.e., $d_f = \lambda_2/4$) [16]. After that, when the frequency (and k_0) further increases, additional passband and stopband appear due to the periodic nature of the trigonometric functions in (4) and (6), that is, the periodicity and cutoff frequencies of the filter response depend on the period p and stub length d_f as they are in the arguments of these functions. The corresponding simulated dispersion curves of the corrugated slotline with variable stub lengths are shown in Fig. 5. The simulation results were obtained using a CST Studio Suite eigenmode solver with a periodic boundary condition, and the structure of the simulated TL corresponds to that of the proposed filtering antenna element.

In addition to dispersion, the periodic TLs have their own characteristic impedance, called Bloch impedance (Z_B), which can be obtained from the ABCD parameters by [17]

$$Z_B = Z_{01}\bar{Z}_B = Z_{01}\sqrt{\frac{B}{C}} \tag{7}$$

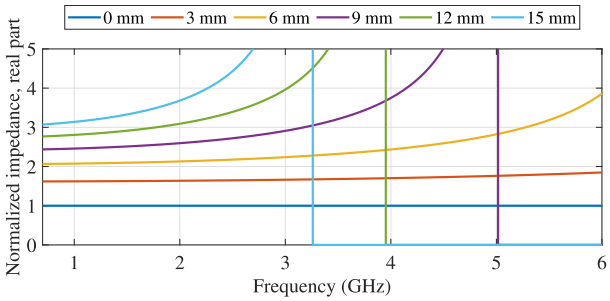

Fig. 6. Normalized Bloch impedances (real part) with different stub lengths d_f. The width of the slotline is 0.77 mm, corresponding to the dimensions of the corrugated Vivaldi element at the location of the deepest stub. Other dimensions are shown in Table I. The vertical lines are asymptotic lines showing the cutoff frequency of the TL.

where B and C are given by (3). After substitution and simplification of B and C, the Bloch impedance becomes

$$Z_B = Z_{01}\sqrt{\frac{2j\sin(\beta_1 p) + \bar{Z}_2(1+\cos(\beta_1 p))}{2j\sin(\beta_1 p) - \bar{Z}_2(1-\cos(\beta_1 p))}}. \tag{8}$$

However, due to the periodic nature of the TL, the input impedance depends on the feed port position. Using (7), the impedance in a different position (inside period p) can be calculated by [17]

$$Z'_B = \frac{Z_B + j\tan\beta_1 s}{1 + jZ_B\tan\beta_1 s} \tag{9}$$

where $s \in [-p/2, p/2]$ is the shift in the feed position. The variation of the Bloch impedance inside the period is not high, except for the high-impedance region near the cutoff frequency. Nevertheless, it does not affect the feeding arrangements if the corrugation is properly tapered.

The real part of the normalized Bloch impedance with different stub lengths is shown in Fig. 6, according to the analytical equations (7) and (8). Note that the stub length is physical length, i.e., it considers the effective dielectric constant of the PCB-based slotline. The real impedances are related to propagating waves and imaginary impedances to evanescent waves. The real Bloch impedance rapidly increases near the cutoff frequency and then transforms to an imaginary number. Obviously, the matching of the periodic TL to the unloaded TL is not trivial due to the frequency-dependent impedance.

C. Finline

A PCB-based Vivaldi element and waveguide form together a finline structure, which is a waveguide structure similar to a double-ridged waveguide [29]. Its cutoff frequency is lower than that of a simple rectangular waveguide, which makes it a suitable structure for wideband antennas.

In Fig. 7, the yellow line represents the dispersion of the simple unloaded finline structure. The line begins near $k_0 = \pi/32$, which corresponds to a 1.1-GHz cutoff frequency. For reference, the red line represents the waveguide without the slotline section, and its cutoff frequency is ca. 4.3 GHz. Thus, the finline considerably lowers the cutoff frequency of the waveguide and provides the 3.8:1 fractional bandwidth before the emergence of the conventional waveguide mode.

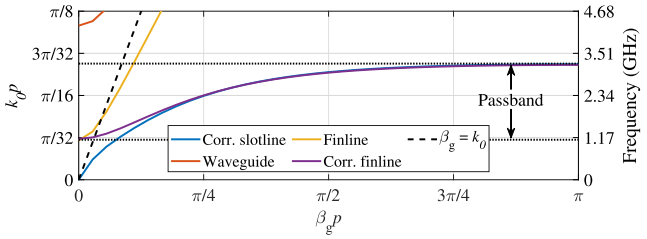

Fig. 7. $\beta_g p - k_0 p$ diagram of different TLs. In this case, the width of the slotline is 0.77 mm, corresponding to the dimensions of the corrugated finline at the location of the deepest stub. Other dimensions are shown in Table I. The black dotted line shows the passband of the proposed corrugated finline structure.

D. Finline-Fed Corrugated Vivaldi Antenna

The combination of tapered, densely corrugated slotline with a waveguide constructs a finline-fed Vivaldi antenna, which is shown in Fig. 2(b) and (c). The length of the waveguide part is determined based on the desired roll-off: a longer waveguide provides a steeper transition band. However, in the proposed antenna, the Vivaldi slot is tapered already inside the waveguide. As the width of the slot inside the waveguide is proportional to the cutoff frequency, the waveguide should end before the slot width becomes significant.

Despite the finline and the corrugated slotline having their own functions in the bandpass filter, their operation cannot be separated and analyzed fully individually. The effect of these parts on the dispersion curve is shown in Fig. 7. The finline itself has a dispersion relation near $k_0 = \beta_g$ curve, and its cutoff is at 1.1 GHz. The corrugated slotline, in turn, has its upper cutoff at ca. 3.2 GHz. The combination of these approximately follows the finline curve in the lower end and the corrugated slotline curve in the upper end. However, there are also small differences: the lower cutoff is at the same frequency, but the dispersion curve has a longer horizontal section implying a steeper roll-off.

The slots are tapered at both ends of the slotline in order to obtain a smooth impedance transition between the slotline/free space and corrugated slotline [17], [20]. In the lower end, the slots are tapered by the Gaussian profile, and in the upper end, the slots are naturally tapered by the exponential opening of the Vivaldi element. In addition to the impedance matching, the tapering of the slots also widens the stopband of the filter structure, as the shorter slots are effective at higher frequencies. Equally long slots would not only have a bad matching to the normal slotline but also a periodic filter response [22].

III. Unit-Cell Simulations

The unit-cell simulations were conducted in CST Studio Suite 2022. In the unit-cell configuration, the simulation problem is equivalent to the antenna element in an infinite antenna array. Thus, the simulation results describe the operation of a typical center element in a large antenna array.

The infinite array simulation provides four parameters that are further studied in the following: active reflection coefficient (ARC), coupling between the orthogonal feed ports, embedded element patterns (EEPs), and efficiency.

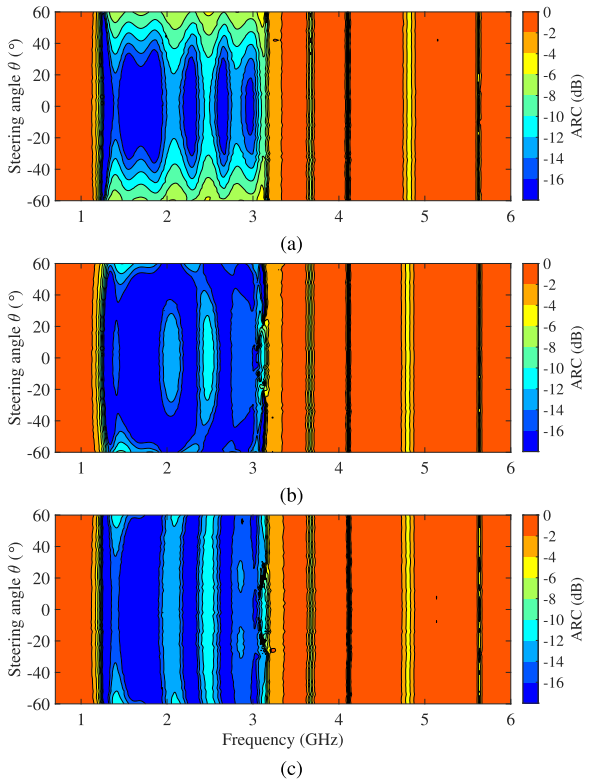

Fig. 8. Simulated ARC of an infinite array in (a) H-plane ($\phi = 0°$), (b) E-plane ($\phi = 90°$), and (c) D-plane ($\phi = 45°$).

A. ARC and Coupling

The simulated ARC of the infinite array is shown in Fig. 8. The ARC is given in the H-plane ($\phi = 0°$), E-plane ($\phi = 90°$), and intercardinal D-plane ($\phi = 45°$). In the passband (1.2–3.1 GHz), the active reflection is very small, less than −10 dB in E- and D-planes (inside ±60° beam-steering range) and less than −6 dB in the H-plane. In the stopband region, the ARC is mainly greater than −2 dB, apart from the deep dips that are caused by nonradiative resonances in the antenna structure, that is, the dips in the ARC are only due to resistive losses, which can be confirmed by the total efficiency analyzed in Section III-C. In general, these kinds of internal, lossy resonant modes are possible at higher frequencies since the antenna structure itself is large with respect to the wavelength. These resonances have strong currents and electric fields that are highly dissipative.

The coupling between the feeding ports of two different polarizations is shown in Fig. 9 in the D-plane. In the passband region, the coupling is negligible at small beam-steering angles and it increases up to −10 dB when the beam is steered to ±60°. In general, the obtained coupling level is typical for Vivaldi arrays. Obviously, as the antenna array does not radiate in the stopband region, also the coupling is negligible, mostly below −40 dB.

B. Embedded Element Patterns

The EEPs define the beam-steering properties of a large antenna array. For an infinite array, it is defined by [33]

$$g(\theta, \phi) = \frac{4\pi A_{\text{phys}}}{\lambda_0^2} \cos\theta (1 - |\text{ARC}(\alpha, \beta)|^2) \qquad (10)$$

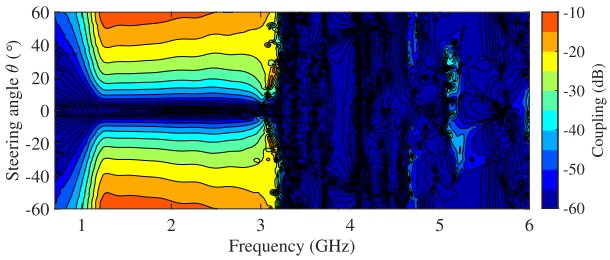

Fig. 9. Active cross-coupling of the orthogonal feed ports of the infinite array in the D-plane ($\phi = 45°$).

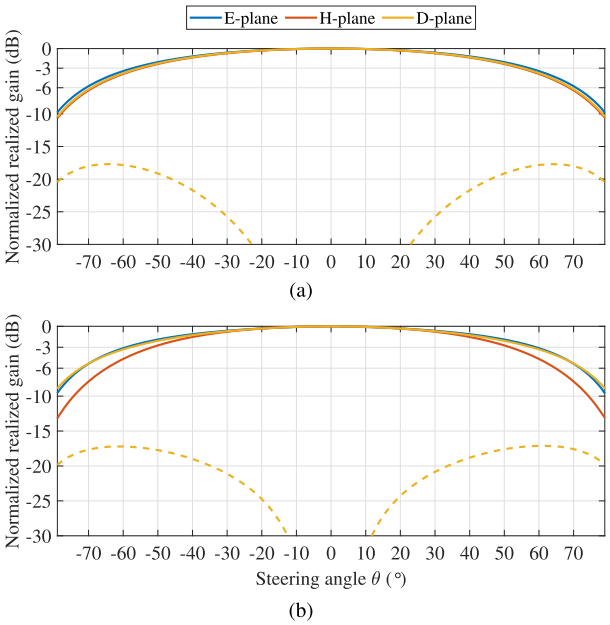

Fig. 10. Simulated EEPs of an infinite array at (a) 1.5 and (b) 3.0 GHz. Co- and cross-polarized components are drawn by solid and dashed lines, respectively.

where A_{phys} is the physical area of one antenna element, λ_0 is the wavelength in free space, and $ARC(\alpha, \beta)$ is the steering-vector-dependent ARC. Thus, the EEP of an ideally matched array without grating lobes would follow a cosine curve.

The EEPs of the proposed antenna array element are shown in Fig. 10, where co- and cross-polarization EEPs are given at 1.5 and 3.0 GHz in three different planes. Ludwig's third definition [34] for polarization is used throughout this article. At 1.5 GHz, the scan loss is nearly ideal in all planes, i.e., only slightly greater than the ideal 3-dB scan loss at ±60°. At 3.0 GHz, the scan loss is also nearly ideal in the E- and D-planes, but considerably worse in the H-plane. This is due to the deteriorating active impedance matching of the antenna array.

The cross-polarization level of the proposed element is slightly smaller than that of conventional Vivaldi elements. At 3.0 GHz, the cross-polarization component of the EEP is at least 14 dB lower than the co-polarized component. Typically, the Vivaldi elements of this height exhibit −11 dB cross-pol/co-pol ratio [31].

C. Efficiency

The total efficiency of the infinite antenna array is shown in Fig. 11. In terms of total efficiency, the antenna array

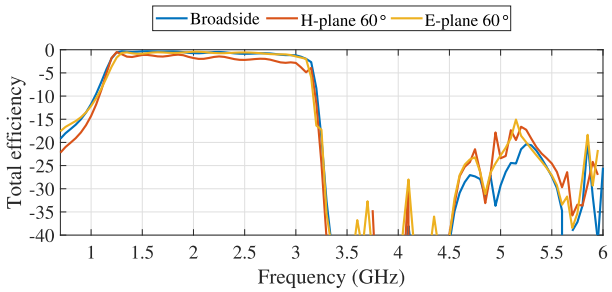

Fig. 11. Simulated total efficiency of the infinite array.

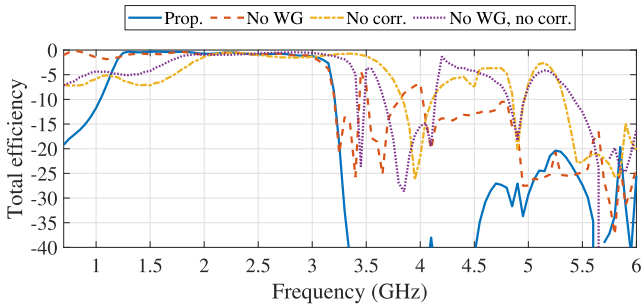

Fig. 12. Simulated total efficiency for the broadside beam with four different antenna configurations.

provides ca. 20-dB attenuation at the stopband. Near the upper edge of the passband, the attenuation is even better than 40 dB. Evidently, the filtering response does not significantly depend on the beam-steering angle.

In filters, the steepness of the transition band is an important factor. In the proposed antenna, the high-pass section of the filter is based on the waveguide. Thus, the roll-off factor, in part, depends on the length of the waveguide. The proposed filtering antenna provides a moderate roll-off that is equivalent to a standard 4th-order 0.5-dB Chebyshev filter. At the upper edge of the passband, the periodic slotline acts as an LPF section. The roll-off is considerably higher as the attenuation increases 31 dB within the 3.1–3.3-GHz transition band. This, in turn, is equivalent to a 16th-order 0.5-dB Chebyshev filter when compared to the ideal case.

The effect of the waveguide (HPF) and corrugation (LPF) are investigated in Fig. 12. Here, the total efficiency of the infinite array is plotted in four different scenarios: the proposed antenna element, antenna element without waveguide, antenna element without corrugation, and antenna element without waveguide and corrugation. It is shown that the waveguide improves the performance of the LPF section and the corrugation improves the roll-off of the HPF section. Furthermore, both filter sections affect the impedance matching. The waveguide improves the attenuation of the LPF because it prevents the radiation of the slotline in unwanted directions. The corrugation, in turn, improves the roll-off of the HPF since it alters the dispersion properties of the whole finline structure, as shown in Fig. 7.

The stopband of the filter can be done very wide if the period of the corrugated slotline is small and the corrugation is tapered properly [22]. However, in Fig. 11, the attenuation is considerably lower near 5.2 GHz. This is not due to

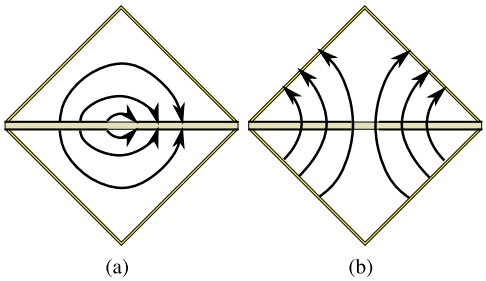

Fig. 13. Sketch of (a) fundamental mode in the finline at in-band frequencies and (b) higher order waveguide mode near 5.2 GHz.

the periodic nature of the filter, but due to higher order waveguide modes in the antenna element. The electric field of the fundamental mode propagating in the finline is shown in Fig. 13(a). In this fundamental mode, the electric field vectors are across the slot. In Fig. 13(b), the higher order waveguide mode is illustrated. This situation corresponds to the radiation of the proposed antenna near 5.2 GHz. Since the electric field is not across the slot anymore, the corrugation of the slot has no effect. Thus, to guarantee the filtering performance of the antenna element, the coupling to the higher order modes should be prevented. In the proposed antenna element, the coupling is minimized by using a stripline feed, which creates the electric field across the slotline and minimizes the coupling to the higher order waveguide mode. However, the slot and balun structure still excite the higher order mode to some extent.

IV. Full-Array Results

A dual-polarized 6 × 6 antenna array shown in Fig. 1 was manufactured and measured in order to confirm the operation of the designed array. The antenna array was measured by a vector network analyzer (VNA) and MVG StarLab 6-GHz antenna measurement device. StarLab is a spherical near-field scanner that provides a fast and accurate measurement of 3-D far-field patterns and total efficiency.

The ARC, passive S-parameters, and EEPs are shown only for selected ports whose locations are shown in Fig. 14. The far-field patterns of all elements were measured and the results were combined numerically to compute beam-steering patterns, total efficiency, and cross-polarization pattern of the complete array.

A. S-Parameters

The passive S-parameters are often not interesting from the array performance viewpoint since the array elements are not used individually. However, passive S-parameters provide information about coupling and reflection coefficients, which may be beneficial when analyzing the operation of the array.

The passive reflection coefficients of a few selected antenna elements are shown in Fig. 15(a). Both measured and simulated full-array S-parameters are given. The results indicate that the edge and corner elements perform worse than the center elements. An interesting fact is also that the reflection coefficient of the central elements is below −10 dB also in a passive scenario. This is not a common property with Vivaldi

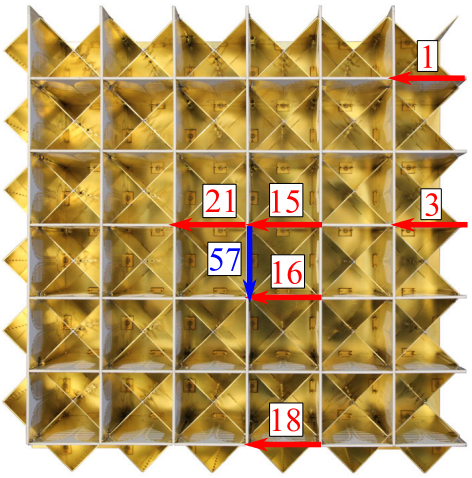

Fig. 14. Element numbering.

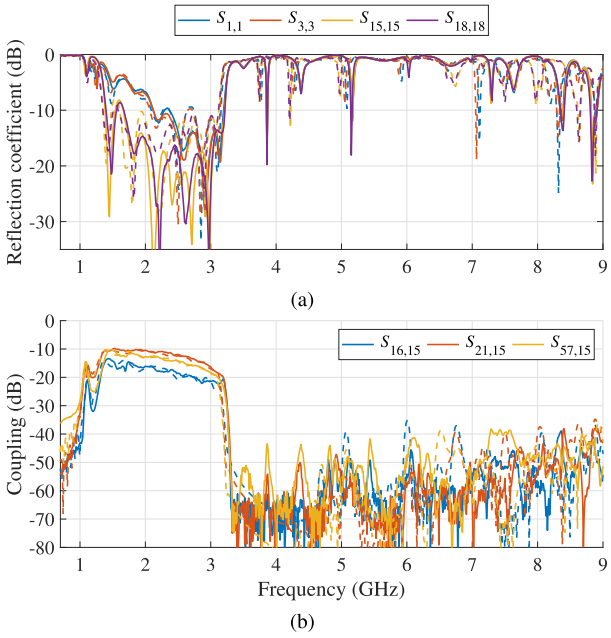

Fig. 15. Measured and simulated passive (a) reflection coefficients and (b) coupling coefficients of the full 6 × 6 antenna array. Simulation results are denoted by a dashed line.

arrays, and it implies that the proposed antenna element is not very sensitive to finite array effects.

Fig. 15(b) shows the passive coupling for the adjacent element in the E- and H-planes, and the cross-coupling of two antenna elements with orthogonal polarizations. The H-plane coupling is significantly lower than the E-plane coupling, which explains, in part, the worse ARC in the H-plane. As the antenna elements of the array have individual filters, the coupling from one element to another also describes the filtering performance. It can be seen that the magnitude difference between the passband and stopband is up to 60 dB, which corresponds to the 30-dB attenuation of one antenna element. However, this estimate is inaccurate since the magnitude of the coupling coefficient is near the noise floor of the VNA.

Generally, the measured S-parameters follow well the simulated ones, which confirms the indented operation of the manufactured prototype.

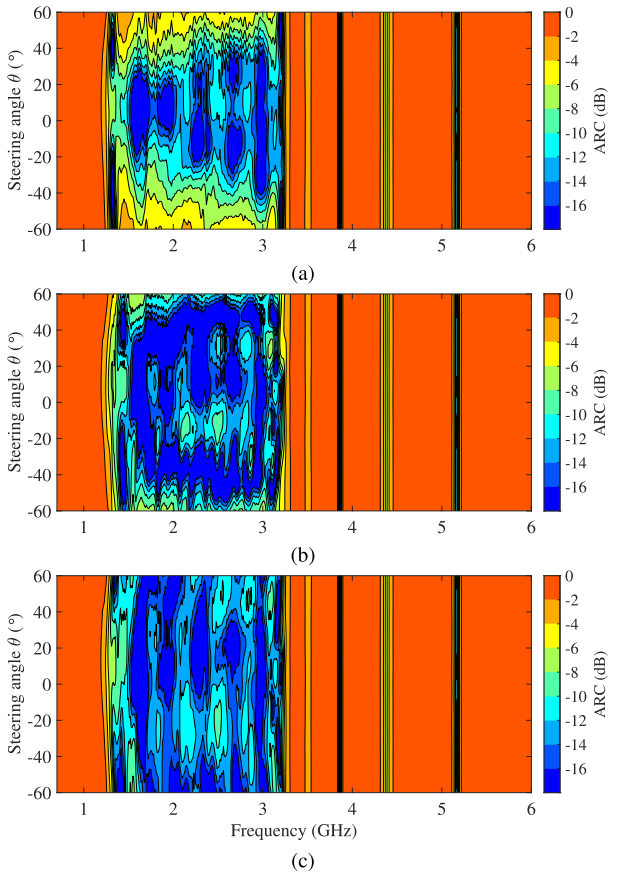

Fig. 16. Measured ARC of port 15 in (a) H-plane, (b) E-plane, and (c) D-plane. Progressive phase shift and uniform amplitude distribution were used.

B. Active Reflection Coefficient

The ARC was computed for element 15, which is the central element in the array. All coupling coefficients to port 15 and the reflection coefficient of port 15 were measured, and the ARC was computed numerically using uniform amplitude distribution and progressive phase shifting using [35]

$$ARC_m = \sum_{n=1}^{N} S_{mn} \frac{a_n}{a_m} \tag{11}$$

where S_{mn} is the measured S-parameter between ports m and n and their excitation coefficients are denoted by a_m and a_n, respectively.

The measured ARC for all beam-steering angles and frequencies is shown in Fig. 16. As with unit-cell simulations, the ARC is given in H-, E-, and D-planes. The measurement results show very similar behavior to the unit-cell simulations, but the level of the reflection is higher. This is a normal phenomenon for small antenna arrays [36].

C. Far-Field Measurements

1) Embedded Element Patterns: The EEP of element 15 was measured in MVG StarLab when other elements were terminated to 50 Ω. In Fig. 17, the EEPs are given in H-, E-, and D-planes at 1.5 and 3.0 GHz. The EEP follows reasonably well the simulated infinite array EEP, although there are some

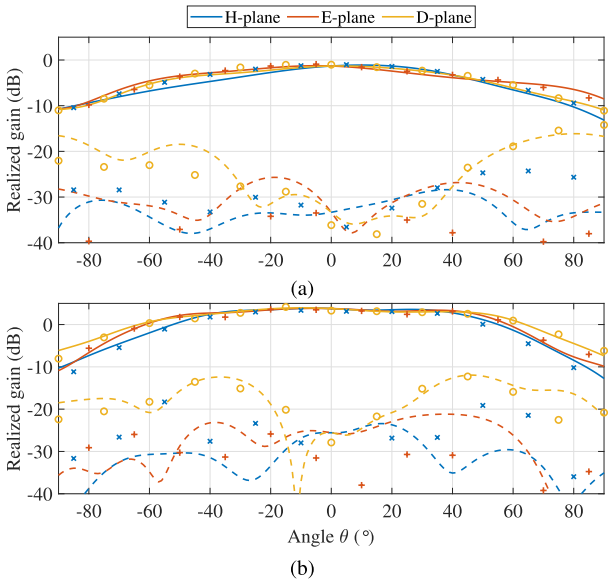

Fig. 17. Measured and simulated EEPs of element 15 at (a) 1.5 and (b) 3.0 GHz. Co- and cross-polarized components are drawn by solid and dashed lines, respectively. Crosses (x), plus signs (+), and circles (o) show the simulated values in H-, E-, and D-planes, respectively.

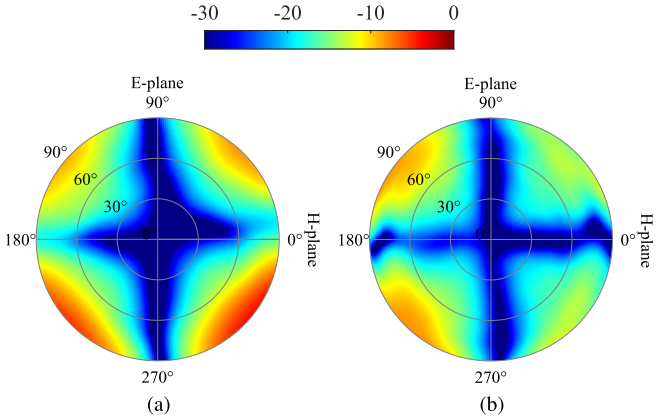

Fig. 18. Measured CPR of the 6 × 6 array at (a) 1.5 and (b) 3.0 GHz.

discrepancies due to the limited array size. The deviation is somewhat larger at a lower frequency when the array is also electrically smaller. Note that the measured element patterns are slightly asymmetric since element 15 is not exactly in the center of the array. Furthermore, the whole array is also asymmetric, as shown in Fig. 14.

2) Cross-Polarization Ratio: The cross-polarization ratio (CPR) of the whole array is presented in Fig. 18. Obviously, the CPR of the array is the largest in the intercardinal D-planes. When $\theta = 60°$, the maximum CPR is −12 dB at 1.5 GHz and −13 dB at 3.0 GHz. Considering the height of the antenna element, the CPR value is reasonable [31], even slightly better than that of conventional Vivaldi arrays. The improved CPR result is aligned with the outcomes of [27], where the corrugation in the inner side of the Vivaldi flare was used to improve the polarization performance of the array. The small asymmetry in the measured CPR pattern is probably due to the asymmetry of the array: since the array is relatively small, the asymmetric edges have a significant effect on the radiation pattern.

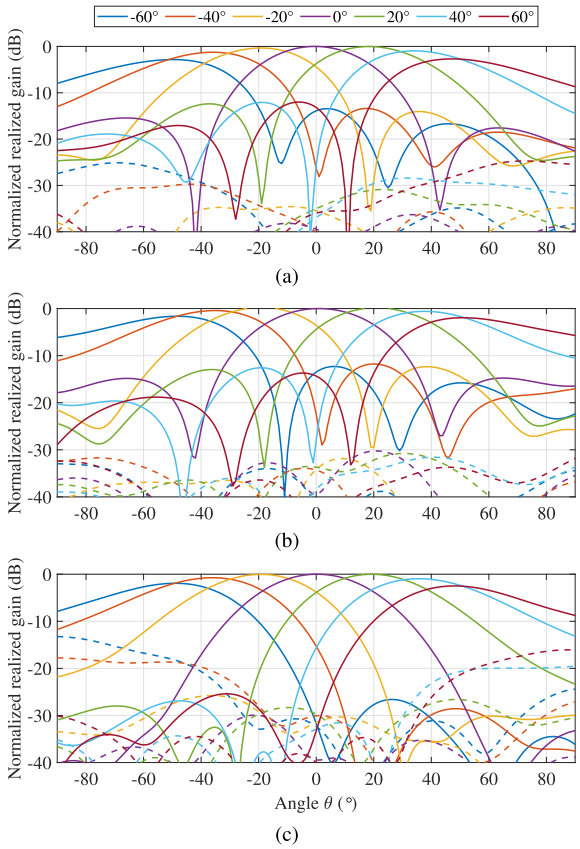

Fig. 19. Measured beam-steering patterns in (a) H-plane, (b) E-plane, and (c) D-plane at 1.5 GHz. Progressive phase shift and uniform amplitude distribution were used. Co- and cross-polarized components are drawn by solid and dashed lines, respectively.

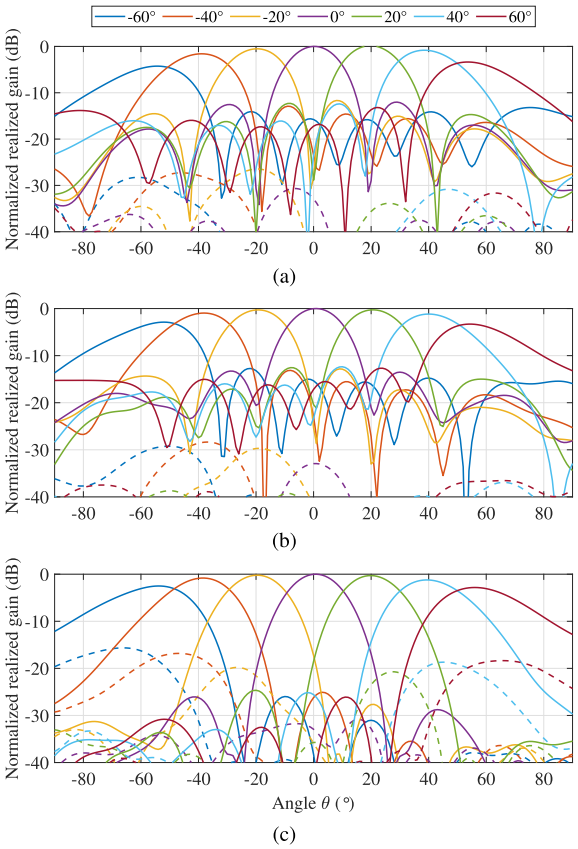

Fig. 20. Measured beam-steering patterns in (a) H-plane, (b) E-plane, and (c) D-plane at 3.0 GHz. Progressive phase shift and uniform amplitude distribution were used. Co- and cross-polarized components are drawn by solid and dashed lines, respectively.

3) Beam-Steering Patterns: The normalized beam-steering patterns were computed from individual EEPs of each element, and they are shown in Figs. 19 and 20 at 1.5 and 3.0 GHz, respectively. Uniform amplitude distribution and progressive phase shifting were used. As the individual patterns are different for each element, the beam-steering patterns do not correspond to the EEP of element 15, but the edge effects of this small array are considered.

The direction of the maximum gain follows the desired beam-steering direction up to ±40°. Due to the small number of elements and scan loss (EEP), the direction of the maximum gain differs 5°–10° when the desired beam-steering direction is set to ±60°. Despite that, the scan loss is pretty small, as shown in Fig. 21. At 1.5 GHz, the 3-dB scan loss level of the co-polarized component is achieved at $\theta = 65°$–$66°$ in the E-plane and $\theta = 56°$ in the H-plane. According to (10), the scan loss of an ideally matched, infinite array at $\theta = 60°$ is 3 dB. Since this scan loss level is achieved at higher steering angle in the E-plane, it implies that the matching of the array elements is worse at $\theta = 0°$ than $\theta \approx 60°$. At 3.0 GHz, the 3-dB scan loss level is at $\theta = 57°$ and $\theta = 52°$–$56°$ in the E- and H-planes, respectively. Considering the finite array effects, these values approximately follow the results of the unit-cell simulation.

D. Efficiency and Realized Gain

In external microwave filters, the filter performance is usually characterized by its two-port S-parameters. However, in the case of filtering antennas, other figures of merit should be used. A good choice is to use the realized gain and total efficiency of the antenna to define its frequency response. However, the total efficiency of the antenna may be a misleading parameter since there might be a sharp beam with considerable realized gain. Thus, the attenuation is more reliably obtained by investigating the maximum realized gain to any direction at each frequency.

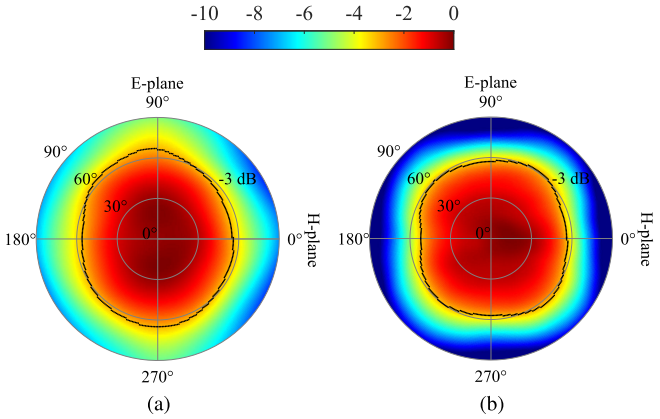

Fig. 21. Measured, normalized co-polarization scan patterns of the 6 × 6 array at (a) 1.5 and (b) 3.0 GHz. The black line shows a 3-dB scan loss level.

In Fig. 22, the total efficiency of the antenna array is presented as a function of frequency and beam-steering angle.

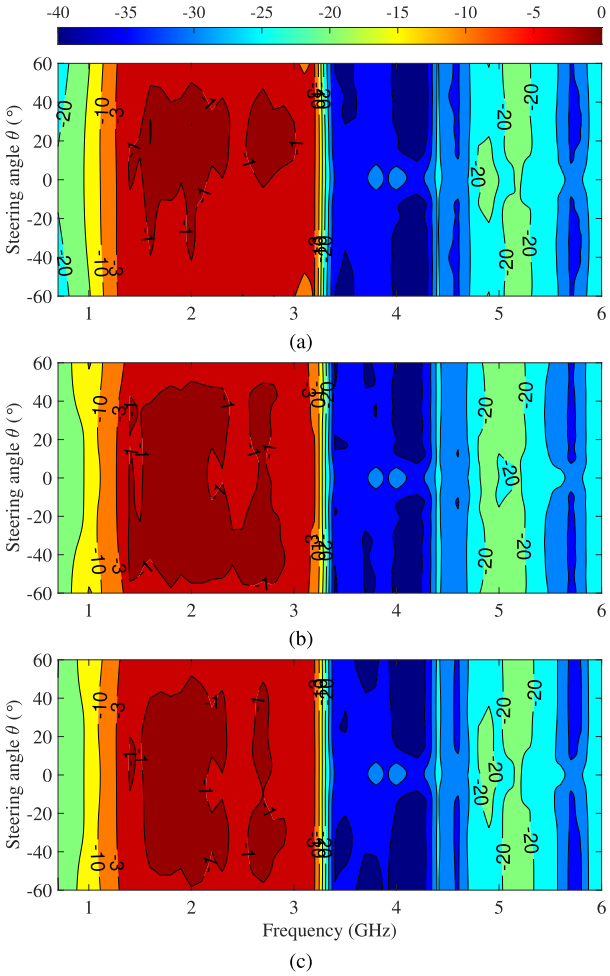

Fig. 22. Measured total efficiency of the whole array in (a) H-plane, (b) E-plane, and (c) D-plane. Progressive phase shift and uniform amplitude distribution were used.

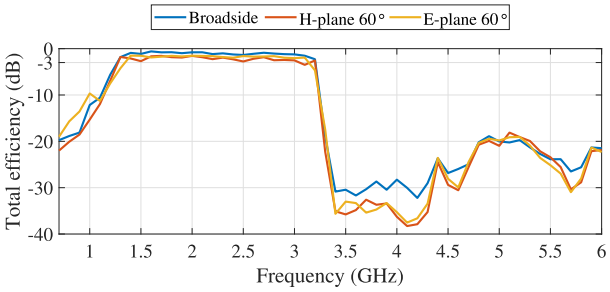

Fig. 23. Measured total efficiency.

Fig. 22 shows that the filter response is pretty flat and the transition band is steep. One important observation is that the filter response is almost independent of the scan angle. In Fig. 23, the total efficiency is plotted in three different beam-steering scenarios. As can be seen, the attenuation is over 30 dB just above the transition band and decreases to 20 dB at 5 GHz.

The measured maximum realized gain is presented in Fig. 24. The results are computed using uniform amplitude and phase distributions corresponding to the broad-side beam. The realized gain curve follows the shape of the total

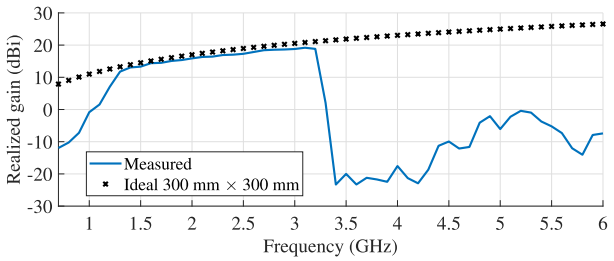

Fig. 24. Maximum realized gain of the full 6 × 6 array when the main beam points to the broadside direction. The black crosses show the directivity of an ideal 300 mm × 300 mm aperture for comparison.

efficiency, indicating that no sharp beams are pointing toward any direction. When the realized gain is compared to the theoretical directivity of a 300 × 300 mm aperture, the filter attenuation is ca. 25 dB in the upper stopband region.

V. Conclusion

This article proposes and investigates a filtering antenna array with a bandpass filtering response. The antenna array consists of a finline structure, whose slot is corrugated. The waveguide, in combination with the corrugated slotline, construct a wideband bandpass filter, which is an integral part of the proposed filtering antenna array.

The proposed filtering antenna array provides wide passband and stopband responses, and steep roll-off. The ARC and beam-steering capability are excellent in E- and D-planes. In the H-plane, the performance is worse due to deteriorated active impedance matching. The polarization performance is good in the class of Vivaldi antennas, and it is not strictly dependent on the frequency.

To the authors' knowledge, the proposed antenna array is the first example of filtering Vivaldi arrays employing a periodic slotline structure. In this light, the proposed array has been designed such that it demonstrates the working principle and opportunities of the proposed filter structure comprehensively. For example, the antenna dimensions are selected so that the proposed array has as wide bandwidth as possible. Of course, narrowed bandwidths are possible by altering the dimensions, and the upper and lower cutoff frequencies can be defined almost independently.

Due to the novelty of the proposed structure, there is much future research to be conducted. For example, some interesting research topics are given as follows:

1) the miniaturization of the antenna array;
2) designing a simpler structure that enables low-cost industrial manufacturing;
3) improving the filtering properties, e.g., by preventing the excitation of higher order waveguide modes.

The proposed antenna array, with possible derivatives, is an interesting option to be used, for example, in radar systems, passive sensors, and other radio devices, where the filtering of out-of-band transmission/reception is important. In the current form, however, the proposed array is probably not the best option for high-power or multiple-input–multiple-output applications due to its losses and high mutual coupling.

ACKNOWLEDGMENT

The authors would like to thank Antti Kuhlberg for assisting with the manufacturing of the antenna. This research was conducted in a collaboration between Aalto University and Saab AB.

REFERENCES

[1] P. P. Shome, T. Khan, S. K. Koul, and Y. M. M. Antar, "Filtenna designs for radio-frequency front-end systems: A structural-oriented review," *IEEE Antennas Propag. Mag.*, vol. 63, no. 5, pp. 72–84, Oct. 2021.

[2] C.-K. Lin and S.-J. Chung, "A filtering microstrip antenna array," *IEEE Trans. Microw. Theory Techn.*, vol. 59, no. 11, pp. 2856–2863, Nov. 2011.

[3] P. F. Hu, Y. M. Pan, X. Y. Zhang, and S. Y. Zheng, "Broadband filtering dielectric resonator antenna with wide stopband," *IEEE Trans. Antennas Propag.*, vol. 65, no. 4, pp. 2079–2084, Apr. 2017.

[4] Y. Zhang, W. Yang, Q. Xue, J. Huang, and W. Che, "Broadband dual-polarized differential-fed filtering antenna array for 5G millimeter-wave applications," *IEEE Trans. Antennas Propag.*, vol. 70, no. 3, pp. 1989–1998, Mar. 2022.

[5] H. Hu and C. H. Chan, "Substrate-integrated-waveguide-fed wideband filtering antenna for millimeter-wave applications," *IEEE Trans. Antennas Propag.*, vol. 69, no. 12, pp. 8125–8135, Dec. 2021.

[6] C. Mao et al., "An integrated filtering antenna array with high selectivity and harmonics suppression," *IEEE Trans. Microw. Theory Techn.*, vol. 64, no. 6, pp. 1798–1805, Jun. 2016.

[7] C. Mao, S. Gao, Y. Wang, F. Qin, and Q. Chu, "Multimode resonator-fed dual-polarized antenna array with enhanced bandwidth and selectivity," *IEEE Trans. Antennas Propag.*, vol. 63, no. 12, pp. 5492–5499, Dec. 2015.

[8] Y. Zhang, X. Y. Zhang, L. Ye, and Y. Pan, "Dual-band base station array using filtering antenna elements for mutual coupling suppression," *IEEE Trans. Antennas Propag.*, vol. 64, no. 8, pp. 3423–3430, Aug. 2016.

[9] Y. Zhang, S. Zhang, G. Yang, and G. F. Pedersen, "A wideband filtering antenna array with harmonic suppression," *IEEE Trans. Microw. Theory Techn.*, vol. 68, no. 10, pp. 4327–4339, Oct. 2020.

[10] R. H. Mahmud and M. J. Lancaster, "High-gain and wide-bandwidth filtering planar antenna array-based solely on resonators," *IEEE Trans. Antennas Propag.*, vol. 65, no. 5, pp. 2367–2375, May 2017.

[11] R. Chen, S. Wong, G. Huang, Y. He, and L. Zhu, "Bandwidth-enhanced high-gain full-metal filtering slot antenna array using TE_{101} and TE_{301} cavity modes," *IEEE Antennas Wireless Propag. Lett.*, vol. 20, no. 10, pp. 1943–1947, Oct. 2021.

[12] H. Cheng, Y. Yusuf, and X. Gong, "Vertically integrated three-pole filter/antennas for array applications," *IEEE Antennas Wireless Propag. Lett.*, vol. 10, pp. 278–281, 2011.

[13] J. Lu et al., "Broadband dual-polarized waveguide slot filtenna array with low cross polarization and high efficiency," *IEEE Trans. Antennas Propag.*, vol. 67, no. 1, pp. 151–159, Jan. 2019.

[14] A. Vosoogh, M. S. Sorkherizi, A. U. Zaman, J. Yang, and A. A. Kishk, "An integrated Ka-band diplexer-antenna array module based on gap waveguide technology with simple mechanical assembly and no electrical contact requirements," *IEEE Trans. Microw. Theory Techn.*, vol. 66, no. 2, pp. 962–972, Feb. 2018.

[15] F.-C. Chen, J.-F. Chen, Q.-X. Chu, and M. J. Lancaster, "X-band waveguide filtering antenna array with nonuniform feed structure," *IEEE Trans. Microw. Theory Techn.*, vol. 65, no. 12, pp. 4843–4850, Dec. 2017.

[16] A. F. Harvey, "Periodic and guiding structures at microwave frequencies," *IEEE Trans. Microw. Theory Techn.*, vol. MTT-8, no. 1, pp. 30–61, Jan. 1960.

[17] R. E. Collin, *Foundations for Microwave Engineering*. New York, NY, USA: McGraw-Hill, 1966.

[18] D. M. Pozar, *Microwave Engineering*, 4th ed. Hoboken, NJ, USA: Wiley, 2012.

[19] W. X. Tang, H. C. Zhang, H. F. Ma, W. X. Jiang, and T. J. Cui, "Concept, theory, design, and applications of spoof surface plasmon polaritons at microwave frequencies," *Adv. Opt. Mater.*, vol. 7, no. 1, Jan. 2019, Art. no. 1800421.

[20] H. Liu, Z. Wang, Q. Zhang, H. Ma, B. Ren, and P. Wen, "Design wideband differential bandpass filter using slotline surface plasmon polaritons," *IEEE Access*, vol. 7, pp. 44212–44218, 2019.

[21] D. Guan, P. You, Q. Zhang, K. Xiao, and S. Yong, "Hybrid spoof surface plasmon polariton and substrate integrated waveguide transmission line and its application in filter," *IEEE Trans. Microw. Theory Techn.*, vol. 65, no. 12, pp. 4925–4932, Dec. 2017.

[22] D. Yi, X. Wei, R. Yang, R. X. Gao, and Y. Yang, "Modeling and analyzing high-order modes in periodic-stub-loaded stripline for wide-band filter design," *IEEE Trans. Electromagn. Compat.*, vol. 62, no. 2, pp. 398–405, Apr. 2020.

[23] J. Y. Yin, H. C. Zhang, Y. Fan, and T. J. Cui, "Direct radiations of surface plasmon polariton waves by gradient groove depth and flaring metal structure," *IEEE Antennas Wireless Propag. Lett.*, vol. 15, pp. 865–868, 2016.

[24] W. Feng, Y. Feng, W. Yang, W. Che, and Q. Xue, "High-performance filtering antenna using spoof surface plasmon polaritons," *IEEE Trans. Plasma Sci.*, vol. 47, no. 6, pp. 2832–2837, Jun. 2019.

[25] H. C. Zhang et al., "A wide-angle broadband converter: From odd-mode spoof surface plasmon polaritons to spatial waves," *IEEE Trans. Antennas Propag.*, vol. 67, no. 12, pp. 7425–7432, Dec. 2019.

[26] Z. Zheng, F. Chen, and F. Xu, "The end-fire Vivaldi antenna based on spoof surface plasmon polaritons," *Microw. Opt. Technol. Lett.*, vol. 63, no. 11, pp. 2870–2875, Nov. 2021.

[27] C. Kolitsidas, "Next generation wideband antenna arrays for communication and radio astrophysics," Ph.D. dissertation, KTH Roy. Inst. Technol., Stockholm, Sweden, 2017.

[28] P. J. Gibson, "The Vivaldi aerial," in *Proc. 9th Eur. Microw. Conf.*, Sep. 1979, pp. 101–105.

[29] P. J. Meier, "Integrated fin-line millimeter components," *IEEE Trans. Microw. Theory Techn.*, vol. MTT-22, no. 12, pp. 1209–1216, Dec. 1974.

[30] J. Shin and D. H. Schaubert, "A parameter study of stripline-fed Vivaldi notch-antenna arrays," *IEEE Trans. Antennas Propag.*, vol. 47, no. 5, pp. 879–886, May 1999.

[31] J. T. Logan, R. W. Kindt, and M. N. Vouvakis, "Low cross-polarization Vivaldi arrays," *IEEE Trans. Antennas Propag.*, vol. 66, no. 4, pp. 1827–1837, Apr. 2018.

[32] H. Holter, T.-H. Chio, and D. H. Schaubert, "Elimination of impedance anomalies in single- and dual-polarized endfire tapered slot phased arrays," *IEEE Trans. Antennas Propag.*, vol. 48, no. 1, pp. 122–124, Jan. 2000.

[33] P. Hannan, "The element-gain paradox for a phased-array antenna," *IEEE Trans. Antennas Propag.*, vol. AP-12, no. 4, pp. 423–433, Jul. 1964.

[34] A. Ludwig, "The definition of cross polarization," *IEEE Trans. Antennas Propag.*, vol. AP-21, no. 1, pp. 116–119, Jan. 1973.

[35] R. C. Hansen, *Phased Array Antennas*, 2nd ed. Hoboken, NJ, USA: Wiley, 2009.

[36] H. Holter and H. Steyskal, "On the size requirement for finite phased-array models," *IEEE Trans. Antennas Propag.*, vol. 50, no. 6, pp. 836–840, Jun. 2002.

Matti Kuosmanen was born in Iisalmi, Finland, in 1996. He received the B.Sc. (Tech.) and M.Sc. (Tech.) degrees in electrical engineering from Aalto University, Espoo, Finland, in 2019 and 2021, respectively. He is currently pursuing the D.Sc. (Tech.) degree with Saab Finland Oy, Helsinki, Finland, and the Department of Electronics and Nanoengineering, School of Electrical Engineering, Aalto University.

His current research interests include wideband, beam-steerable antenna arrays, and characteristic mode analysis.

Jari Holopainen received the M.Sc. degree from the Helsinki University of Technology, Espoo, Finland, in 2005, the D.Sc. degree in electrical engineering from Aalto University, Espoo, in 2011, and the teacher's pedagogic qualification from the Häme University of Applied Sciences, Hämeenlinna, Finland, in 2015.

He is currently a Senior University Lecturer with the Department of Electronics and Nanoengineering, School of Electrical Engineering, Aalto University. His current research interests include antennas and RF-powered devices.

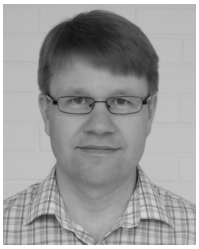

Juha Ala-Laurinaho received the Diploma Engineering (M.Sc.) degree in mathematics and the D.Sc. (Tech.) degree in electrical engineering from the TKK Helsinki University of Technology, Espoo, Finland, in 1995 and 2001, respectively.

He has been with Aalto University, formerly TKK, where he was with the Radio Laboratory from 1995 to 2007 and the Department of Radio Science and Engineering from 2008 to 2016 and is currently with the Department of Electronics and Nanoengineering. He works as a Staff Scientist. He has been a Researcher and a Project Manager in various millimeter-wave technology-related projects. His current research interests are the antennas and antenna measurement techniques for millimeter and submillimeter waves, and millimeter-wave imaging.

Tero Kiuru received the M.Sc. (Tech.) degree in electrical engineering from the TKK Helsinki University of Technology, Espoo, Finland, in 2006, and the D.Sc. (Tech.) degree (Hons.) in electrical engineering from Aalto University, Espoo, in 2011.

He has worked at the Department of Radio Science and Engineering, Aalto University; the European Space Agency's Research Centre ESTEC, Noordwijk, The Netherlands; NASA's Jet Propulsion Laboratory, Pasadena, CA, USA; the VTT Technical Research Centre of Finland, Espoo; and Saab Finland Oy, Helsinki, Finland. He is currently a Research Leader with Saab Finland Oy. He has over 15 years of experience in research activities in high-frequency radio technology, radar technology, and electronic warfare systems. He has published more than 40 scientific articles in the fields of microwave components and systems, radar technologies, and high-frequency measurements. His current research interests include novel microwave radar and electronic warfare systems.

Ville Viikari (Senior Member, IEEE) received the Master of Science (Tech.) and Doctor of Science (Tech.) (Hons.) degrees in electrical engineering from the Helsinki University of Technology (TKK), Espoo, Finland, in 2004 and 2007, respectively.

From 2001 to 2007, he was with the Radio Laboratory, TKK (now part of Aalto University), where he studied antenna measurement techniques at submillimeter wavelengths and antenna pattern correction techniques. From 2007 to 2012, he was a Research Scientist and a Senior Scientist with the VTT Technical Research Centre, Espoo, where his research included wireless sensors, RFID, radar applications, MEMS, and microwave sensors. He was appointed as an Assistant Professor at Aalto University, Espoo, in 2012. He is currently a Professor and the Deputy Head of the Department of Electronics and Nanoengineering, School of Electrical Engineering, Aalto University. He has authored or coauthored more than 90 journal articles and 100 conference papers. He is an inventor of 16 granted patents. His current research interests include antennas for mobile devices and networks, antenna clusters and coupled arrays, RF-powered devices, and antenna measurement techniques.

Dr. Viikari is a regional delegate of The European Association on Antennas and Propagation (EurAAP). He was a recipient of the Young Researcher Award of the Year 2014 presented by the Finnish Foundation for Technology Promotion and the IEEE Sensors Council 2010 Early Career Gold Award.